



Article

Charge Transport Enhancement in BiVO₄ Photoanode for Efficient Solar Water Oxidation

Zhidong Li, Zhibin Xie, Weibang Li, Hafiz Sartaj Aziz, Muhammad Abbas, Zhuanghao Zheng, Zhenghua Su, Ping Fan, Shuo Chen *  and Guangxing Liang * 

Shenzhen Key Laboratory of Advanced Thin Films and Applications, Key Laboratory of Optoelectronic Devices and Systems of Ministry of Education and Guangdong Province, College of Physics and Optoelectronic Engineering, Shenzhen University, Shenzhen 518060, China

* Correspondence: chensh@szu.edu.cn (S.C.); lgx@szu.edu.cn (G.L.)

Abstract: Photoelectrochemical (PEC) water splitting in a pH-neutral electrolyte has attracted more and more attention in the field of sustainable energy. Bismuth vanadate (BiVO₄) is a highly promising photoanode material for PEC water splitting. Additionally, cobaltous phosphate (CoPi) is a material that can be synthesized from Earth's rich materials and operates stably in pH-neutral conditions. Herein, we propose a strategy to enhance the charge transport ability and improve PEC performance by electrodepositing the in situ synthesis of a CoPi layer on the BiVO₄. With the CoPi co-catalyst, the water oxidation reaction can be accelerated and charge recombination centers are effectively passivated on BiVO₄. The BiVO₄/CoPi photoanode shows a significantly enhanced photocurrent density (J_{ph}) and applied bias photon-to-current efficiency (ABPE), which are 1.8 and 3.2 times higher than those of a single BiVO₄ layer, respectively. Finally, the FTO/BiVO₄/CoPi photoanode displays a photocurrent density of 1.39 mA cm⁻² at 1.23 V_{RHE}, an onset potential (V_{on}) of 0.30 V_{RHE}, and an ABPE of 0.45%, paving a potential path for future hydrogen evolution by solar-driven water splitting.

Keywords: BiVO₄; photoanode; electro-deposition; water oxidation; catalyst



Citation: Li, Z.; Xie, Z.; Li, W.; Aziz, H.S.; Abbas, M.; Zheng, Z.; Su, Z.; Fan, P.; Chen, S.; Liang, G. Charge Transport Enhancement in BiVO₄ Photoanode for Efficient Solar Water Oxidation. *Materials* **2023**, *16*, 3414. <https://doi.org/10.3390/ma16093414>

Academic Editor: Igor R. Iatsunskyi

Received: 3 April 2023

Revised: 24 April 2023

Accepted: 25 April 2023

Published: 27 April 2023



Copyright: © 2023 by the authors. Licensee MDPI, Basel, Switzerland. This article is an open access article distributed under the terms and conditions of the Creative Commons Attribution (CC BY) license (<https://creativecommons.org/licenses/by/4.0/>).

1. Introduction

The production of hydrogen through solar-driven water splitting typically stores solar energy in chemical bonds, which is a potential strategy for overcoming shortages of energy and related global environmental problems [1–5]. The characteristics of photoanode materials decide the solar-to-hydrogen (STH) efficiency of a photoelectrochemical (PEC) device, because the kinetic demand of oxygen evolution reaction (OER) in the PEC water-splitting procedure is higher than the hydrogen evolution reaction (HER) [6–8]. To date, various neutral electrolytes have been studied to function as PEC photoanodes, such as TiO₂ [9,10], Fe₂O₃ [11], WO₃ [12], and BiVO₄ [13–18]. Among them, the monoclinic bismuth vanadate (BiVO₄) has received significant attention because of its favorable band-edge positions, its moderate band gap energy (E_g , 2.4–2.5 eV) [19], low cost, etc. However, the surface charge recombination and severe bulk defect delay the OER kinetics limits PEC performance [20]. BiVO₄ photoanodes have been the subject of numerous studies aimed at enhancing their PEC performance, including doping [21], building heterojunction [22], crystal facet or morphology engineering [23], oxygen vacancies (O_v) introduction, and the surface modification of oxygen evolution catalysts (OECs), etc. [24,25].

The surface modification of oxygen evolution catalysts is a more promising method for enhancing the PEC performance of BiVO₄ photoanodes than its other counterparts, due to the effective passivation of the surface charge recombination centers and improving the interfacial OER kinetics for PEC water oxidation. For instance, J. Hu et al. successfully synthesized iron oxyhydroxide (FeOOH) with different crystalline phases (α -, β -, and δ -) through a regulated solvothermal pathway, where the electrocatalytic OER activity of β -FeOOH was highest [26]. Carbon quantum dots (CQDs) are also able to remarkably

improve electrocatalytic OER activity owing to the increased O_v density; at the same time, they can form heterojunctions with semiconductors, thereby effectively promoting charge separation and transport [27]. Moreover, L. Wu et al. synthesized the nickel boride (NiB) layer by adjusting the composition of the neutral electrolyte. The borates with B-O bonds become promoters of catalyst activity by accelerating proton-coupled electron transfer and interact with Ni^{2+} ions to inhibit charge recombination on $BiVO_4$ surface, thereby reporting a J_{ph} of 6.0 mA cm^{-2} at 1.23 V_{RHE} [14]. Cobaltous phosphate (CoPi) is an effective electrocatalyst for water oxidation and was first reported by G. Nocera and W. Kanan, who also demonstrated that hydrogen phosphate ions are proton acceptors in oxygen production reactions under neutral pH conditions [28]. Moreover, J. Durrant et al. discussed the oxidation degree of the CoPi catalyst on the $BiVO_4$ photoanode under simulated sunlight irradiation and determined the appropriate degree of catalyst oxidation to drive substantial water oxidation. Additionally, the relative kinetics of water oxidation on the surfaces of electrocatalyst and semiconductor and the kinetics of holes transfer to electrocatalysts were discussed for the first time [18].

In this work, a $BiVO_4$ thin film was initially fabricated, which is inherently beneficial for charge transport through the adjustment the electrodeposition time of the BiOI precursor film and the dropping of excessive vanadium source solution for annealing in a muffle furnace. Then, the cobaltous phosphate (CoPi) layer was electrodeposited on optimal $BiVO_4$ electrodes while the composition of neutral electrolyte was regulated by adding cobaltous nitrate and phosphate species. Finally, the FTO/ $BiVO_4$ /CoPi photoanode was successfully prepared. Combining the electrocatalytic and photoelectric technologies, the CoPi for OER catalytic activity was investigated in detail and notable results were obtained, e.g., a J_{ph} of 1.39 mA cm^{-2} (at 1.23 V_{RHE}) and an undoped ABPE of 0.45% under AM 1.5 G illumination.

2. Materials and Methods

2.1. Preparation of BiOI Precursor Film

The BiOI precursor film was electrodeposited on an FTO glass substrate with an effective area of $1.5 \text{ cm} \times 2 \text{ cm}$ in a three-electrode system, where a Pt-foil was used as the counter electrode and an Ag/AgCl with saturated KCl solution was used as the reference electrode. The BiOI precursor deposition solution was fabricated by dissolving lactic acid (0.03 M), KI (0.4 M), and $Bi(NO_3)_3 \cdot 5H_2O$ (0.015 M) in deionized water (100 mL), with 1,4-Benzoquinone (0.046 M) in ethanol (40 mL) solution. The pH of the mixed solution was adjusted to 3.7 by adding 0.1 M nitric acid aqueous solution after stirring for 20 min. Initially, a 60 s deposition was conducted at $-0.40 \text{ V}_{Ag/AgCl}$ to prevent the falling off of BiOI films from the surface of the FTO substrate. After the initial deposition, the BiOI film was obtained at a constant voltage of $-0.25 \text{ V}_{Ag/AgCl}$ with different deposition durations, then rinsed thoroughly with deionized water and dried in a drying oven.

2.2. Preparation of $BiVO_4$ Electrode

The vanadium source solution was prepared by dissolving $VO(acac)_2$ (0.5 M) in dimethylsulfoxide (10 mL). The as-prepared BiOI precursor film was dropped into the superfluous vanadium source solution. The electrode was then shifted to a muffle furnace and annealed for about 12 h. The heating rate was $3 \text{ }^\circ\text{C}/\text{min}$ to $120 \text{ }^\circ\text{C}$, $0.67 \text{ }^\circ\text{C}/\text{min}$ to $280 \text{ }^\circ\text{C}$, and $1.41 \text{ }^\circ\text{C}/\text{min}$ to $450 \text{ }^\circ\text{C}$, and then held at $450 \text{ }^\circ\text{C}$ for 1 h. All the annealing processes ended with furnace cooling. After annealing, the electrodes were immersed in a 1.0 M NaOH solution for 15 min with gentle stirring to wash off the V_2O_5 on the $BiVO_4$ surface. The prepared $BiVO_4$ electrodes were rinsed thoroughly with deionized water and dried in a drying oven.

2.3. Photo-Assisted Electrodeposition of CoPi Cocatalyst

The CoPi cocatalyst was electrodeposited on the $BiVO_4$ electrode under AM 1.5 G simulated sunlight by using the three-electrode system containing the solutions of NaH_2PO_4 (0.1 M), Na_2HPO_4 (0.1 M), $Co(NO_3)_2 \cdot 6H_2O$ (0.001 M), and deionized water (100 mL). Simi-

larly, an Ag/AgCl with a saturated KCl solution was used as the reference electrode and a Pt-foil as the counter electrode. The deposition voltage and time were $-0.40 V_{\text{Ag/AgCl}}$ and 90 s, respectively.

2.4. Characterizations

The crystallinity and structure of BiVO_4 films were examined by X-ray diffraction (XRD, Ultima-iv with $\text{Cu}/\text{K}\alpha$ radiation). Surface morphologies were observed via scanning electron microscope (SEM, Germany Zeiss SUPRA 55). The transmittance and absorption of BiVO_4 films were measured via a Shimadzu UV-3600 spectrophotometer. Ultraviolet photoelectron spectroscopy (UPS) was performed using a PHI 5000 VersaProbe with an energy value of a He I source with 21.22 eV. The PEC performance was obtained by using the CHI 660E electrochemical workstation under a three-electrode system, where an Ag/AgCl with saturated KCl solution was used as the reference electrode, with Pt-foil as the counter electrode and the BiVO_4 photoanode as the working electrode. Photoelectrochemical impedance spectroscopy (PEIS) was assessed under light conditions, and its frequency ranged from 10^{-1} Hz to 10^5 Hz. Mott-Schottky (M-S) measurements were used to calculate the flat band potential (E_{fb}) of the BiVO_4 films and the analysis of defects in junctions formed at the interface of semiconductor electrolytes.

3. Results and Discussion

BiVO_4 film with different thicknesses can be prepared by adjusting the electrodeposition time of the BiOI precursor film, i.e., the BiOI-1 precursor film deposited at 300 s, BiOI-2 at 330 s, and BiOI-3 at 360 s, respectively, and then dropping excessive vanadium source solution to anneal in muffle furnace. The resulting BiVO_4 films were labeled as BiVO_4 -1, BiVO_4 -2, and BiVO_4 -3, and the corresponding thicknesses were 358.5 nm, 424.3 nm, and 485.6 nm, respectively (Figure S1). The X-ray diffraction (XRD) patterns of BiVO_4 film with three different thicknesses are shown in Figure 1a. The existence of three major diffraction peaks (011), (-121), and (040) and the standard monoclinic BiVO_4 (JCPDS Card No.14-0688) peaks without any extra peaks, confirm the high crystallinity and pureness of the as-fabricated BiVO_4 thin films [1]. Figure 1b shows that the smaller FWHM (full width at half maxima) values of different diffraction peaks demonstrate larger crystal grains in the BiVO_4 -2 film. The grain size can also be calculated according to the Scherrer formula [29]:

$$D = \frac{K\lambda}{\beta \cos\theta} \quad (1)$$

where K is the Scherrer constant, λ is the wavelength of the X-ray sources (0.15406 nm), D is crystallite size (nm), β is the FWHM value, and θ is the Bragg angle at peak position. Figure 1c displays the proportion diagram of grain size distribution, and the BiVO_4 -2 obviously accounts for a large proportion in areas with a large grain size distribution. In addition, the average grain sizes of BiVO_4 -1, BiVO_4 -2, and BiVO_4 -3 are 15.54, 16.28, and 15.51 nm, respectively. The surface scanning electron microscopy (SEM) images of the BiVO_4 -1, BiVO_4 -2, and BiVO_4 -3 films are shown in Figure 1d–f. It can be seen that Figure 1e depicts larger crystalline grains compared to those of BiVO_4 -1 (Figure 1d). The BiVO_4 -1 film consists of many small grains with obvious voids on their surfaces, which are not conducive to charge transport, possibly due to the increase in charge recombination centers on the BiVO_4 -1 film surface. On the other hand, a quasi-uniform BiVO_4 -2 film with large grains can be obtained by increasing the deposition time of the BiOI precursor film, which is directly related to its effective thermodynamic/kinetic growth under a sufficient annealing temperature. However, the BiVO_4 -3 film shows a stacked structure and more voids than the BiVO_4 -2 film as the deposition time of the precursor film increases (Figure 1f). Therefore, highly compact and quasi-uniform BiVO_4 -2 films are better for photo-assisted electrodeposition with a CoPi catalyst.

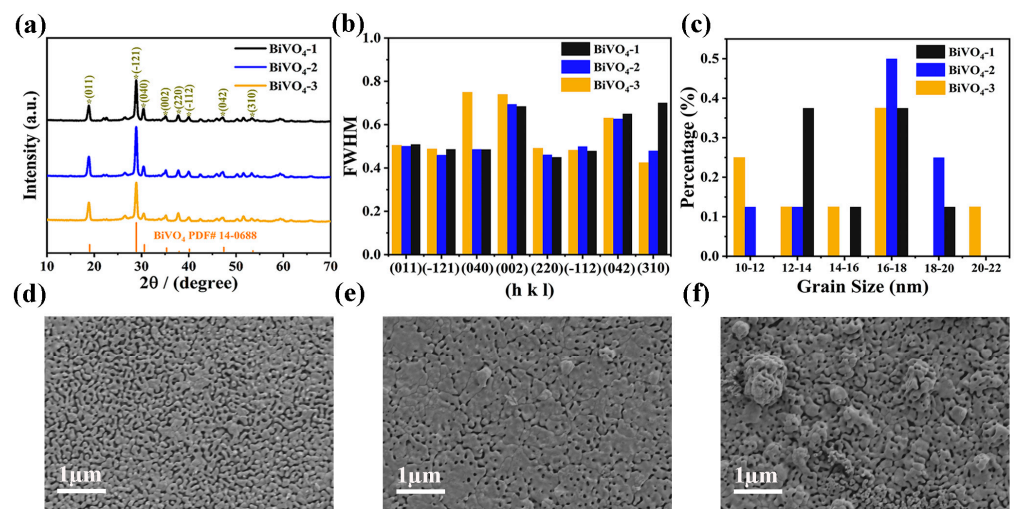


Figure 1. (a) XRD patterns; (b) full width at half maxima of different diffraction peaks; (c) grain size; and (d–f) surface SEM pictures of the BiVO₄ films with different thicknesses.

The energy band gap (E_g) of the BiVO₄ semiconductor was gained from the transmission spectra in the wavelength range of 300 nm to 1500 nm, as shown in Figure 2a. The transmittance value of the BiVO₄-2 film is lower than that of the BiVO₄-1 and BiVO₄-3 films, indicating that it has a higher absorbance. The FTO was used as a substrate, and the E_g value was calculated using the equations below [30]:

$$\alpha = \ln(1/T)/d \quad (2)$$

$$\alpha hv = C(hv - E_g)^n \quad (3)$$

where n is an index equal to 0.5 in a direct band-gap semiconductor, d is the thickness of the BiVO₄ film, T is the transmission, hv is the energy of a photon, α is the absorption coefficient, and C is a constant. The BiVO₄ films with three different thicknesses display a similar E_g value of 2.41 eV (Figure 2b). The energy band information of the BiVO₄ film was calculated via ultraviolet photoelectron spectroscopy (UPS), as we can see in Figure 2c. According to the secondary electron cut-off (SEC) edge and valence band (V_B) position, the work function (Φ) of BiVO₄ was calculated as 5.57 eV [31]; meanwhile, the E_F and E_V are determined as -5.57 eV and -7.23 eV, respectively (Supplementary Materials, Note S1). In combination with its optical band gap (E_g), at a value of 2.41 eV, the conduction band (E_C , vs. vacuum) of the BiVO₄ semiconductor can be obtained, and its value is -4.82 eV.

The photocurrent density potential (J - V) curves of pure BiVO₄ photoanodes with different thicknesses corresponding to the differing BiVO₄/CoPi photoanodes are shown in Figure 2d. It can be seen that the BiVO₄-2 photoanodes are significantly superior to other BiVO₄ photoanodes, indicating that the BiVO₄ film with the fewest charge recombination centers was obtained by adjusting the electrodeposition time of the BiOI precursor film and the annealing temperature. In addition, we can also see that the J_{ph} and the fill factor of all BiVO₄ photoanodes increased after CoPi catalyst surface modification. Of these, the BiVO₄-2/CoPi photoanode has a maximum J_{ph} value of 1.39 mA cm^{-2} . Therefore, BiVO₄-2 with optimal thickness was selected in this work in order to study the effect of CoPi catalyst on OER occurrence and PEC performance. The potential relative to the Ag/AgCl reference electrode ($V_{Ag/AgCl}$) can be converted into V_{RHE} using the Nernst equation [32]:

$$V_{RHE} = V_{Ag/AgCl} + 0.059 \times PH + 0.198 \quad (4)$$

while ABPE was obtained from the J-V response of the photoanodes according to the following equation [33]:

$$\text{ABPE}(\%) = J_{\text{ph}} \times (V_{\text{RHE}} - V_{\text{H}_2\text{O}/\text{O}_2}) / P_{\text{sun}} \times 100\% \quad (5)$$

where V_{RHE} is the potential relative of a relative hydrogen electrode (RHE), $V_{\text{H}_2\text{O}/\text{O}_2}$ is the oxidation potential for oxygen ($1.23 V_{\text{RHE}}$), and P_{sun} is the simulated sunlight intensity ($100 \text{ mW}/\text{cm}^2$). The electrocatalytic OER activities of BiVO_4 and $\text{BiVO}_4/\text{CoPi}$ electrodes were measured by linear sweep voltammetry (LSV) tests in $0.2 \text{ M Na}_2\text{HPO}_4/\text{NaH}_2\text{PO}_4$ solution ($\text{pH} = 6.5$) under dark conditions. Figure 3a depicts the LSV curves with a 100% iR drop compensation and a 0.1 mV s^{-1} scanning rate of the OER catalysts. In general, a catalyst's OER activity is typically evaluated based on its overpotential at a current density of 10 mA cm^{-2} [27]. Therefore, the $\text{BiVO}_4/\text{CoPi}$ displays the overpotential value of $0.99 V_{\text{RHE}}$, which is smaller than that of BiVO_4 ($1.87 V_{\text{RHE}}$) at 10 mA cm^{-2} and the Tafel slope of $\text{BiVO}_4/\text{CoPi}$ ($106.0 \text{ mV dec}^{-1}$) is also obviously lower than that of BiVO_4 ($265.7 \text{ mV dec}^{-1}$), indicating that the CoPi catalyst is able to drive reactions at lower overpotentials and play an excellent role in BiVO_4 surface modification (Figure 3b,c). Moreover, the chopped J-V curves are relevant to photoanodes in the dark and continuous illumination within a lesser potential range ($<1.5 V_{\text{RHE}}$) and are shown in Figure 3d. The dark current density is very low ($\sim 0 \text{ mA cm}^{-2}$ at $1.23 V_{\text{RHE}}$); hence, under AM 1.5 G simulated sunlight illumination, the photocurrent density of BiVO_4 and $\text{BiVO}_4/\text{CoPi}$ photoanodes increases sharply, confirming the rapid photo-generated carrier generation, separation, and transport, without the need for excess drive potentials. The J-V curves based on BiVO_4 and $\text{BiVO}_4/\text{CoPi}$ photoanodes are displayed in Figure 3e. Specifically, the J_{ph} values at $1.23 V_{\text{RHE}}$ are determined to be 0.75 mA cm^{-2} and 1.39 mA cm^{-2} in sequence. Furthermore, Figure 3f exhibits the as-calculated ABPE and the $\text{BiVO}_4/\text{CoPi}$ photoanode (0.45%) is about ~ 3 times higher than the BiVO_4 photoanode (0.14%), indicating a simultaneous upgrade in PEC performance.

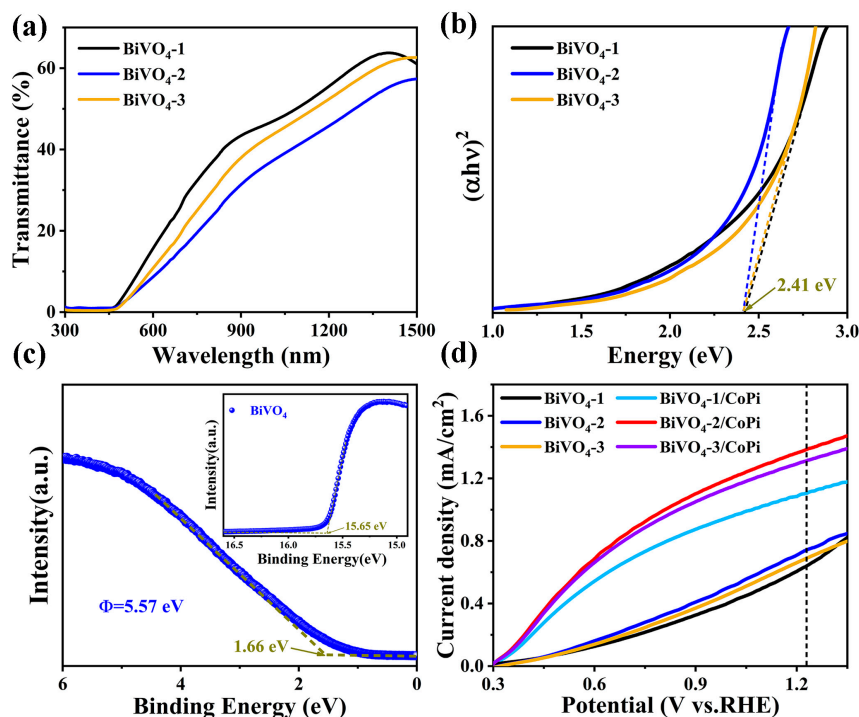


Figure 2. (a) Transmission spectra; (b) plots of $(\alpha hv)^2$ versus energy; (c) UPS characterizations deriving the SEC edge and the V_{B} position of BiVO_4 film; and (d) J-V curves of the BiVO_4 photoanodes with different thicknesses corresponding to differing $\text{BiVO}_4/\text{CoPi}$ photoanodes under sunlight illumination.

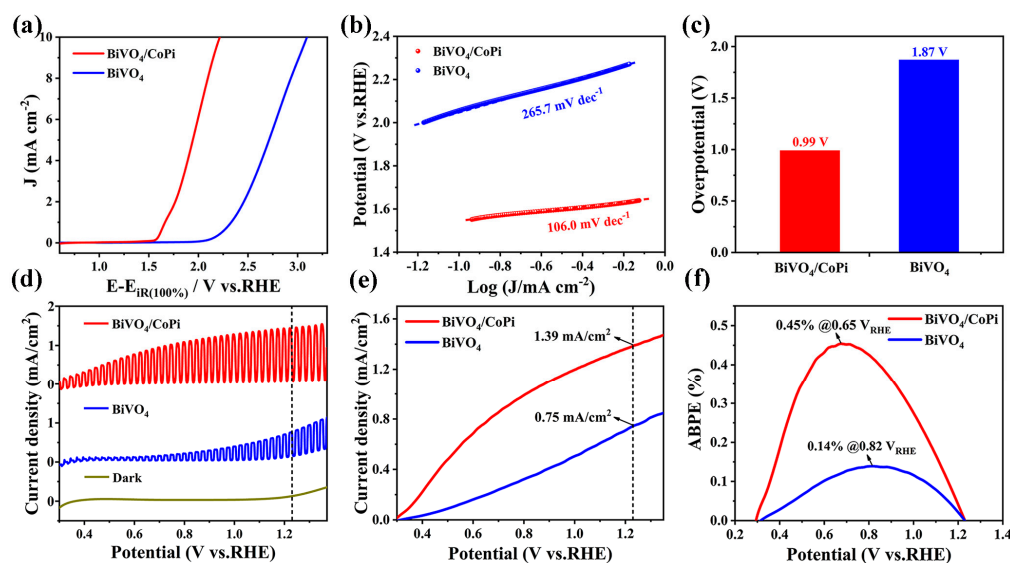


Figure 3. (a) LSV curves with 100% iR drop compensation and a 0.1 mV s^{-1} scanning rate, (b) Tafel plots, and (c) overpotential plots at a current density of 10 mA cm^{-2} of the electrochemical OER measurements with the BiVO_4 and $\text{BiVO}_4/\text{CoPi}$ photoelectrode catalysts in $0.2 \text{ M Na}_2\text{HPO}_4/\text{NaH}_2\text{PO}_4$ solution ($\text{pH} = 6.5$) under dark conditions. (d) J-V curves of the BiVO_4 and $\text{BiVO}_4/\text{CoPi}$ photoanodes under dark conditions and simulated sunlight irradiation; (e) J-V curves of the BiVO_4 and $\text{BiVO}_4/\text{CoPi}$ photoanodes under sunlight illumination. (f) Calculated ABPE values.

The charge transport kinetics were explored according to the electrochemical impedance test. Figure 4a,b exhibits the photoelectrochemical impedance spectroscopy (PEIS) characterization of the BiVO_4 and $\text{BiVO}_4/\text{CoPi}$ photoanodes under illumination. The equivalent circuit is shown in Figure 4a; R_W can be attributed to the resistance of the electrolyte solution, and R_{ct} and C_{sc} represent the charge transport resistance and capacitance in the space charge region of the electrode/electrolyte interface. The fitted results are shown in Table 1, the chi-square values of the BiVO_4 and $\text{BiVO}_4/\text{CoPi}$ photoanodes are both less than 0.02, and we can also see that the raw data and the fitted results match well (Figure 4a). Similar R_W values (18.2–18.8 Ω) indicate the stability of the test environment, and the remarkably smaller R_{ct} value of the $\text{BiVO}_4/\text{CoPi}$ photoanode (137.9 Ω) implies a more effective charge transport at the electrode/electrolyte interface. The larger C_{sc} value of the $\text{BiVO}_4/\text{CoPi}$ photoanode ($5.20 \times 10^{-4} \text{ F}$) indicates that the ability of the charge collection is strengthened. Generally, the PEIS-derived low-frequency region ($10^{-1} \sim 10^1 \text{ Hz}$) normally represents the mass transfer reactions in the electrode/electrolyte interface [34]. As shown in Figure 4b, the reduction of interface impedance ($|Z|$) also proves that the CoPi catalyst accelerates the mass transfer process. Moreover, the peaks in the Bode diagrams for the BiVO_4 photoanode are located at low frequencies ($10^{-1} \sim 10^1 \text{ Hz}$), while the $\text{BiVO}_4/\text{CoPi}$ photoanode is located between 10^1 and 10^2 Hz (insert in Figure 4b). The rapid response of the $\text{BiVO}_4/\text{CoPi}$ photoanode to frequency indicates that charge transport and mass transfer simultaneously accelerated. The Mott–Schottky (M-S) measurement was also introduced in order to study the junction formed at the semiconductor–electrolyte interface in reaction to the applied potential ($V_{\text{Ag}/\text{AgCl}}$, i.e., the aforementioned E_{appl}). Figure 4c reveals that the $1/C^2$ increases with the potential $V_{\text{Ag}/\text{AgCl}}$ in the presence of the space charge region (SCR), indicating n-type properties for the BiVO_4 semiconductor. Moreover, the conduction band position of BiVO_4 semiconductor relative to normal hydrogen electrode (NHE) can be obtained from the flat band potential (E_{fb}), donor density (N_D), the effective density of

states functions in the conduction band (N_c), and the effective mass of the electron (m_n^*), according to the following equations [35,36]:

$$\frac{1}{C_{sc}^2} = \frac{2}{eA^2\epsilon\epsilon_0N_D} \left(E_{appl} - E_{fb} - \frac{k_B T}{e} \right) \tag{6}$$

$$E_c(vs.NHE) = E_{fb} + kT \ln \left(\frac{N_c}{N_D} \right) \tag{7}$$

$$N_c = 2 \left(\frac{2\pi m_n^* kT}{h^2} \right)^{\frac{3}{2}} \tag{8}$$

where C_{sc} is the SCR capacitance in the semiconductor–electrolyte interface, A is the active device area, ϵ_0 is the permittivity of vacuum, ϵ is the relative dielectric coefficient, k_B is Boltzmann constant, e is the unit charge, and T represents the temperature. The E_{fb} value and N_D value of the BiVO_4 are $0.38 V_{NHE}$ and $1.92 \times 10^{21} \text{ cm}^{-3}$, respectively. At room temperature ($T = 25 \text{ }^\circ\text{C}$), the vacuum energy level can be converted to V_{NHE} by the following formula [37,38]:

$$\text{Energy}(vs.vacuum) = -eE_{appl}(vs.NHE) - 4.44 \text{ eV} \tag{9}$$

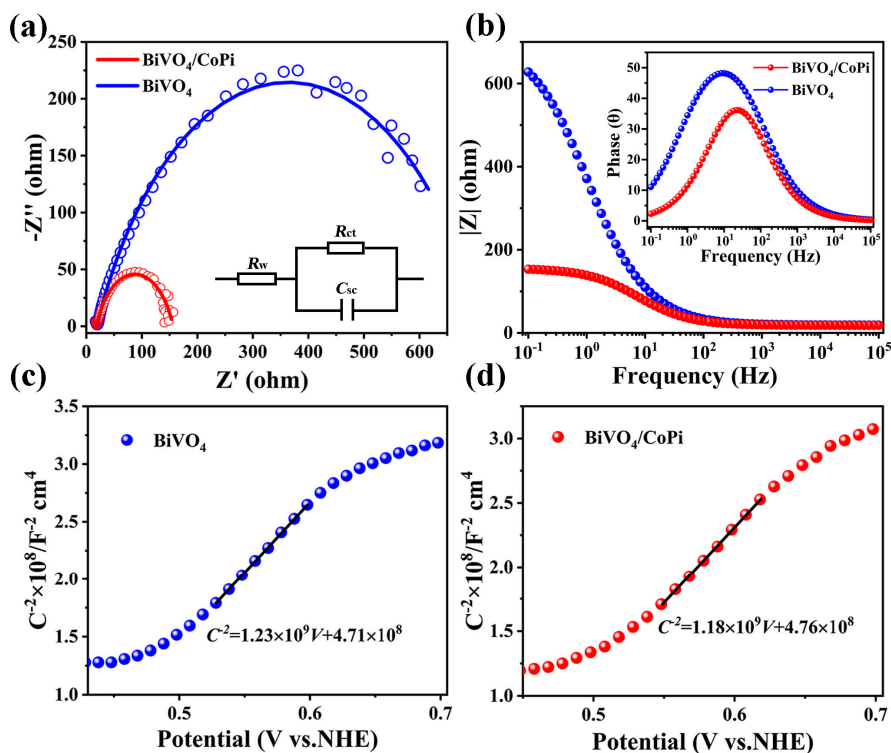


Figure 4. (a) Nyquist plots and equivalent circuit diagram (inset), where the small circles represent the raw data and the solid lines represent the fitting results, and (b) the corresponding Bode plots of the BiVO_4 and $\text{BiVO}_4/\text{CoPi}$ photoanodes. M-S plots of (c) BiVO_4 and (d) $\text{BiVO}_4/\text{CoPi}$ at a 1 kHz frequency.

Table 1. Summary of the PEIS fitted parameters for FTO/ BiVO_4 and FTO/ $\text{BiVO}_4/\text{CoPi}$ photoanodes.

Photoanodes	R_w (Ω)	R_{ct} (Ω)	C_{sc} (F)
FTO/ BiVO_4	18.8	690.3	5.03×10^{-4}
FTO/ $\text{BiVO}_4/\text{CoPi}$	18.22	137.9	5.20×10^{-4}

The calculated E_C value range is -4.82 ± 0.02 eV, using the above equations, which is consistent with the E_C of -4.82 eV obtained from the UPS measurement. According to the E_g value (2.41 eV) calculated by transmission, the valance band (E_V , vs. NHE) is $2.79 V_{NHE}$, which thermodynamically supports the occurrence of water oxidation with oxygen production by solar-driven water splitting. In contrast, the E_{fb} value and N_D value of the $BiVO_4/CoPi$ quasi-semiconductor are $0.40 V_{NHE}$ and $8.87 \times 10^{20} \text{ cm}^{-3}$, respectively (Figure 4d). The lower N_D value demonstrates that the CoPi catalyst passivates defects (e.g., charge recombination centers) on the $BiVO_4$ film surface, reducing electron–hole recombination during charge transport to the electrode/electrolyte interface, thereby improving photocurrent density. We can also clearly observe that the CoPi catalyst effectively reduces the defect pinholes on the $BiVO_4$ surface through a top-view SEM image of the $BiVO_4/CoPi$ photoanode (Figure S2). The increase in E_{fb} of $0.02 V_{NHE}$ also indicates that the $BiVO_4/CoPi$ photoanode is more beneficial for water oxidation in thermodynamics (Figure S3).

The surface charge transfer efficiency (η_{tran}) and bulk charge separation efficiency (η_{sep}) of the $BiVO_4$ photoanode were further investigated in order to determine the reasons for the significantly improved photocurrent density after surface modification with CoPi catalyst. The integrated photocurrent density (J_{abs}) of $BiVO_4$ and $BiVO_4/CoPi$ photoanodes can be obtained according to wavelength-dependent light harvesting efficiency (LHE) and the standard AM 1.5 G solar spectrum, utilizing the following formulas [1]:

$$J_{abs} = \int_{300}^{\lambda_e} \frac{\lambda}{1240} \cdot N_{ph}(\lambda) \cdot LHE(\lambda) d\lambda \quad (10)$$

$$LHE = 1 - 10^{-A(\lambda)} \quad (11)$$

where J_{abs} is the integrated photocurrent density, λ_e is the absorption cut-off wavelength that is linked to the band gap, $N_{ph}(\lambda)$ is the photo flux, and $A(\lambda)$ is the wavelength-dependent absorption, covering wavelengths from 350 to 800 nm (Figure 5a). The λ_e values for $BiVO_4$ and $BiVO_4/CoPi$ were determined to be at 514 nm and 520 nm, suggesting CoPi can also effectively broaden and heighten the LHE range of the $BiVO_4$ photoanode (Figure 5b), and giving the J_{abs} values of 6.29 mA cm^{-2} and 6.68 mA cm^{-2} , respectively (Figure 5c). Moreover, the transient photocurrent response spectra of the $BiVO_4$ and $BiVO_4/CoPi$ photoanodes are shown in Figure 5d, while the η_{tran} can be obtained through the measured photocurrents associated with the “light off” state and the “light on” state, according to the following formulas [32]:

$$\eta_{tran} = \frac{J_{ss}}{J_{inst}} \quad (12)$$

where J_{ss} is the photocurrent density in steady state and J_{inst} signifies the instantaneous photocurrent density. Accordingly, the η_{tran} value of the $BiVO_4/CoPi$ photoanode (82.1%) has increased in comparison to the $BiVO_4$ photoanode (76.0%), demonstrating that the CoPi catalyst accelerates holes transfer to the electrode/electrolyte interface and then oxidizes water. Moreover, we can observe in Figure 5d that the $BiVO_4/CoPi$ photoanode has a spike peak in the “light off” state compared with the $BiVO_4$ photoanode. The negative current transient suggests that there is significant back electron/hole recombination after “light off” [39], reiterating that the $BiVO_4/CoPi$ photoanode has a larger capacitance value (Table 1), which demonstrates that the CoPi catalyst can delay charge recombination and promote the OER’s continuous progress. Additionally, the η_{sep} can be calculated using following equation [32]:

$$\eta_{sep} = \frac{J_{ph}}{J_{abs} \times \eta_{tran}} \quad (13)$$

The $BiVO_4$ and $BiVO_4/CoPi$ photoanodes’ calculated η_{sep} values are 15.7%, and 25.4%, respectively. The obvious improvement of the η_{sep} value indicates that the CoPi catalyst is also conducive to promoting the rapid separation of electron–hole pairs in the $BiVO_4$ body.

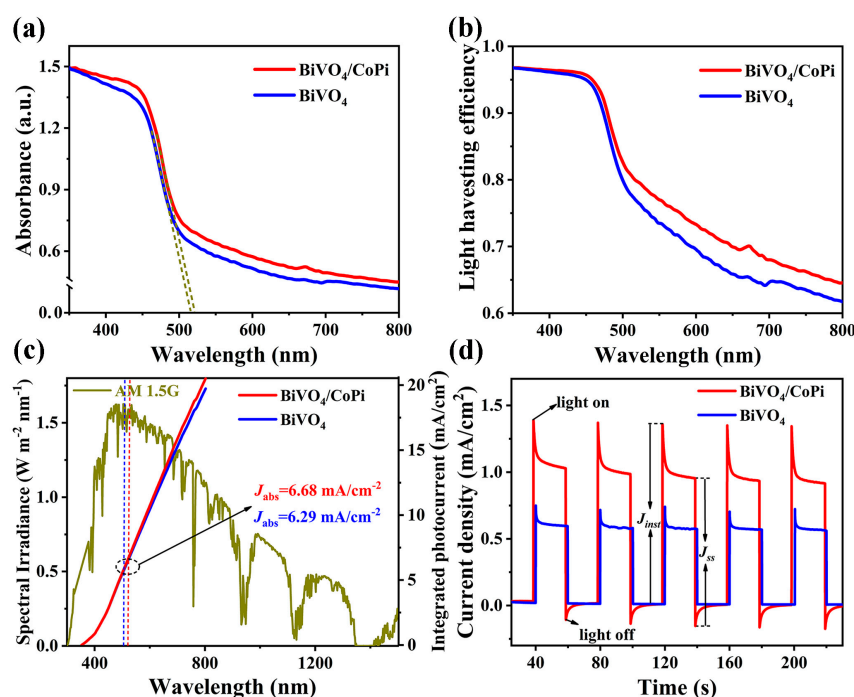


Figure 5. (a) Wavelength-dependent absorbance and (b) the light harvesting efficiency (*LHE*) of the BiVO_4 and $\text{BiVO}_4/\text{CoPi}$ photoanodes. (c) The integrated photocurrent density of the BiVO_4 and $\text{BiVO}_4/\text{CoPi}$ photoanodes, as well as the energy density flux for the standard AM 1.5 G solar spectrum. (d) Transient photocurrent response of the BiVO_4 and $\text{BiVO}_4/\text{CoPi}$ photoanodes.

4. Conclusions

In summary, a highly compact and quasi-uniform BiVO_4 film was obtained at a suitable electrodeposition time and annealing temperature. After the successful electrodeposition of the CoPi catalyst on the optimized BiVO_4 electrode, the FTO/ $\text{BiVO}_4/\text{CoPi}$ photoanodes were fabricated, and their PEC performances were systematically investigated. Due to the surface modification of the CoPi catalyst, i.e., passivating charge recombination centers on the BiVO_4 surface and promoting the separation of electron–hole pairs in the BiVO_4 body, the interface impedance ($|Z|$) of the mass transfer process was decreased, while significantly enhancing the η_{tran} value of 82.1% and η_{sep} value of 25.4%. The J_{ph} and ABPE of the BiVO_4 photoanode were increased by about ~ 2 times and ~ 3 times, respectively, demonstrating that the CoPi catalyst can accelerate holes transfer from the BiVO_4 semiconductor to the catalyst in order to be competitive with water oxidation by holes in the semiconductor and to improve PEC performance. The results of this study may open up the possibility for the future design and construction of extremely effective photoanodes for solar-driven water splitting.

Supplementary Materials: The following supporting information can be downloaded at: <https://www.mdpi.com/article/10.3390/ma16093414/s1>, Figure S1: Cross-sectional SEM images of the (a) BiVO_4 -1, (b) BiVO_4 -2, and (c) BiVO_4 -3 film; Figure S2: Top-view SEM image of the $\text{BiVO}_4/\text{CoPi}$ photoanode; Figure S3: The energy levels schematic diagram of the BiVO_4 and $\text{BiVO}_4/\text{CoPi}$ photoanodes; Supplementary Note S1. UPS analysis.

Author Contributions: Z.L., Z.X. and W.L. contributed equally to this work. Conceptualization, G.L. and S.C.; methodology, Z.L., Z.Z. and Z.S.; validation, P.F.; formal analysis, H.S.A., M.A., G.L. and S.C.; investigation, Z.L., Z.X. and W.L.; writing—original draft preparation, Z.L., Z.X. and W.L.; writing—review and editing, H.S.A., G.L. and S.C.; visualization, P.F.; supervision, G.L. and S.C.; funding acquisition, G.L. and S.C. All authors have read and agreed to the published version of the manuscript.

Funding: This work was supported by National Natural Science Foundation of China (No. 62104156); Guangdong Basic and Applied Basic Research Foundation (2022A1515010979, 2023A1515011256), China; Science and Technology plan project of Shenzhen (20220808165025003, 20200812000347001), China.

Institutional Review Board Statement: Not applicable.

Informed Consent Statement: Not applicable.

Data Availability Statement: The data presented in this study are available on request from the corresponding authors.

Conflicts of Interest: The authors declare no conflict of interest.

References

1. Zhou, T.; Chen, S.; Wang, J.; Zhang, Y.; Li, J.; Bai, J.; Zhou, B. Dramatically enhanced solar-driven water splitting of BiVO₄ photoanode via strengthening hole transfer and light harvesting by co-modification of CQDs and ultrathin β-FeOOH layers. *Chem. Eng. J.* **2021**, *403*, 126350. [[CrossRef](#)]
2. Xiao, J.; Hou, X.; Zhao, L.; Li, Y. A carbon-quantum-dot-sensitized ZnO:Ga/ZnO multijunction composite photoanode for photoelectrochemical water splitting under visible light irradiation. *J. Catal.* **2017**, *346*, 70. [[CrossRef](#)]
3. Yang, Y.; Niu, S.; Han, D.; Liu, T.; Wang, G.; Li, Y. Progress in Developing Metal Oxide Nanomaterials for Photoelectrochemical Water Splitting. *Adv. Energy Mater.* **2017**, *7*, 1700555. [[CrossRef](#)]
4. Benedoue, S.; Benedet, M.; Gasparotto, A.; Gauquelin, N.; Orekhov, A.; Verbeeck, J.; Seraglia, R.; Pagot, G.; Rizzi, G.A.; Balzano, V.; et al. Insights into the Photoelectrocatalytic Behavior of gCN-Based Anode Materials Supported on Ni Foams. *Nanomaterials* **2023**, *13*, 1035. [[CrossRef](#)] [[PubMed](#)]
5. Li, C.; Luo, Z.; Wang, T.; Gong, J. Surface, Bulk, and Interface: Rational Design of Hematite Architecture toward Efficient Photo-Electrochemical Water Splitting. *Adv. Mater.* **2018**, *30*, 1707502. [[CrossRef](#)]
6. Li, Z.; Qu, Y.; Hu, K.; Humayun, M.; Chen, S.; Jing, L. Improved photoelectrocatalytic activities of BiOCl with high stability for water oxidation and MO degradation by coupling RGO and modifying phosphate groups to prolong carrier lifetime. *Appl. Catal. B* **2017**, *203*, 355. [[CrossRef](#)]
7. Zhang, Y.; Li, Y.; Ni, D.; Chen, Z.; Wang, X.; Bu, Y.; Ao, J.P. Improvement of BiVO₄ Photoanode Performance During Water Photo-Oxidation Using Rh-Doped SrTiO₃ Perovskite as a Co-Catalyst. *Adv. Funct. Mater.* **2019**, *29*, 1902101. [[CrossRef](#)]
8. Duan, L.; Tong, L.; Xu, Y.; Sun, L. Visible light-driven water oxidation—From molecular catalysts to photoelectrochemical cells. *Energy Environ. Sci.* **2011**, *4*, 3296. [[CrossRef](#)]
9. Li, Z.; Luo, L.; Li, M.; Chen, W.; Liu, Y.; Yang, J.; Xu, S.M.; Zhou, H.; Ma, L.; Xu, M.; et al. Photoelectrocatalytic C–H halogenation over an oxygen vacancy-rich TiO₂ photoanode. *Nat. Commun.* **2021**, *12*, 6698. [[CrossRef](#)]
10. Cho, I.S.; Logar, M.; Lee, C.H.; Cai, L.; Prinz, F.B.; Zheng, X. Rapid and Controllable Flame Reduction of TiO₂ Nanowires for Enhanced Solar Water-Splitting. *Nano Lett.* **2014**, *14*, 24. [[CrossRef](#)]
11. Shen, S.; Lindley, S.A.; Chen, X.; Zhang, J.Z. Hematite heterostructures for photoelectrochemical water splitting: Rational materials design and charge carrier dynamics. *Energy Environ. Sci.* **2016**, *9*, 2744. [[CrossRef](#)]
12. Ronconi, F.; Syrgiannis, Z.; Bonasera, A.; Prato, M.; Argazzi, R.; Caramori, S.; Cristino, V.; Bignozzi, C.A. Modification of Nanocrystalline WO₃ with a Dicationic Perylene Bisimide: Applications to Molecular Level Solar Water Splitting. *J. Am. Chem. Soc.* **2015**, *137*, 4630. [[CrossRef](#)] [[PubMed](#)]
13. Wang, S.; Chen, P.; Bai, Y.; Yun, J.H.; Liu, G.; Wang, L. New BiVO₄ Dual Photoanodes with Enriched Oxygen Vacancies for Efficient Solar-Driven Water Splitting. *Adv. Mater.* **2018**, *30*, 1800486. [[CrossRef](#)] [[PubMed](#)]
14. Gao, R.T.; Nguyen, N.T.; Nakajima, T.; He, J.; Liu, X.; Zhang, X.; Wang, L.; Wu, L. Dynamic semiconductor-electrolyte interface for sustainable solar water splitting over 600 hours under neutral conditions. *Sci. Adv.* **2023**, *9*, eade4589. [[CrossRef](#)] [[PubMed](#)]
15. Kuang, Y.; Jia, Q.; Nishiyama, H.; Yamada, T.; Kudo, A.; Domen, K. A Front-Illuminated Nanostructured Transparent BiVO₄ Photoanode for >2% Efficient Water Splitting. *Adv. Energy Mater.* **2016**, *6*, 1501645. [[CrossRef](#)]
16. Hanway, P.J.; Winter, A.H. Heteroaryl Oxenium Ions Have Diverse and Unusual Low-Energy Electronic States. *J. Phys. Chem. A* **2016**, *116*, 9398–9403. [[CrossRef](#)]
17. Ma, Y.; Kafizas, A.; Pendlebury, S.R.; Le Formal, F.; Durrant, J.R. Photoinduced Absorption Spectroscopy of CoPi on BiVO₄: The Function of CoPi during Water Oxidation. *Adv. Funct. Mater.* **2016**, *26*, 4951–4960. [[CrossRef](#)]
18. Lu, Y.; Yang, Y.; Fan, X.; Li, Y.; Zhou, D.; Cai, B.; Wang, L.; Fan, K.; Zhang, K. Boosting Charge Transport in BiVO₄ Photoanode for Solar Water Oxidation. *Adv. Mater.* **2022**, *34*, 2108178. [[CrossRef](#)]
19. Kim, J.H.; Lee, J.S. Elaborately Modified BiVO₄ Photoanodes for Solar Water Splitting. *Adv. Mater.* **2019**, *31*, 1806938. [[CrossRef](#)]
20. Han, H.S.; Shin, S.; Kim, D.H.; Park, I.J.; Kim, J.S.; Huang, P.-S.; Lee, J.K.; Cho, I.S.; Zheng, X. Boosting the solar water oxidation performance of a BiVO₄ photoanode by crystallographic orientation control. *Energy Environ. Sci.* **2018**, *11*, 1299–1306. [[CrossRef](#)]
21. Rettie, A.J.E.; Lee, H.C.; Marshall, L.G.; Lin, J.F.; Capan, C.; Lindemuth, J.; McCloy, J.S.; Zhou, J.; Bard, A.J.; Mullins, C.B. Combined Charge Carrier Transport and Photoelectrochemical Characterization of BiVO₄ Single Crystals: Intrinsic Behavior of a Complex Metal Oxide. *J. Am. Chem. Soc.* **2013**, *135*, 11389–11396. [[CrossRef](#)] [[PubMed](#)]

22. Zhang, X.; Zhang, B.; Cao, K.; Brillet, J.; Chen, J.; Wang, M.; Shen, Y. A perovskite solar cell-TiO₂/BiVO₄ photoelectrochemical system for direct solar water splitting. *J. Mater. Chem. A* **2015**, *3*, 21630–21636. [[CrossRef](#)]
23. McDonald, K.J.; Choi, K.-S. A new electrochemical synthesis route for a BiOI electrode and its conversion to a highly efficient porous BiVO₄ photoanode for solar water oxidation. *Energy Environ. Sci.* **2012**, *5*, 8553–8557. [[CrossRef](#)]
24. Vo, T.G.; Tai, Y.; Chiang, C.Y. Novel hierarchical ferric phosphate/bismuth vanadate nanocactus for highly efficient and stable solar water splitting. *Appl. Catal. B* **2019**, *243*, 657–666. [[CrossRef](#)]
25. Zhang, B.; Chou, L.; Bi, Y. Tuning surface electronegativity of BiVO₄ photoanodes toward high-performance water splitting. *Appl. Catal. B* **2020**, *262*, 118267. [[CrossRef](#)]
26. Hu, J.; Li, S.; Chu, J.; Niu, S.; Wang, J.; Du, Y.; Li, Z.; Han, X.; Xu, P. Understanding the Phase-Induced Electrocatalytic Oxygen Evolution Reaction Activity on FeOOH Nanostructures. *ACS Catal.* **2019**, *9*, 10705–10711. [[CrossRef](#)]
27. Li, G.; Hou, S.; Gui, L.; Feng, F.; Zhang, D.; He, B.; Zhao, L. Carbon quantum dots decorated Ba_{0.5}Sr_{0.5}Co_{0.8}Fe_{0.2}O_{3-δ} perovskite nanofibers for boosting oxygen evolution reaction. *Appl. Catal. B* **2019**, *257*, 117919. [[CrossRef](#)]
28. Kanan, M.W.; Nocera, D.G. In situ formation of an oxygen-evolving catalyst in neutral water containing phosphate and Co²⁺. *Science* **2008**, *321*, 1072. [[CrossRef](#)] [[PubMed](#)]
29. Chen, S.; Liu, T.; Chen, M.; Ishaq, M.; Tang, R.; Zheng, Z.; Su, Z.; Li, X.; Qiao, X.; Fan, P.; et al. Crystal growth promotion and interface optimization enable highly efficient Sb₂Se₃ photocathodes for solar hydrogen evolution. *Nano Energy* **2022**, *99*, 107417. [[CrossRef](#)]
30. Joshi, G.P.; Saxena, N.S.; Mangal, R.; Mishra, A.; Sharma, T.P. Band gap determination of Ni-Zn ferrites. *Bull. Mater. Sci.* **2003**, *26*, 387–389. [[CrossRef](#)]
31. Chen, S.; Fu, Y.; Ishaq, M.; Li, C.; Ren, D.; Su, Z.; Qiao, X.; Fan, P.; Liang, G.; Tang, J. Carrier recombination suppression and transport enhancement enable high-performance self-powered broadband Sb₂Se₃ photodetectors. *InfoMat* **2023**, e12400. [[CrossRef](#)]
32. Liang, G.; Liu, T.; Ishaq, M.; Chen, Z.; Tang, R.; Zheng, Z.; Su, Z.; Fan, P.; Zhang, X.; Chen, S. Heterojunction interface engineering enabling high onset potential in Sb₂Se₃/CdS photocathodes for efficient solar hydrogen production. *Chem. Eng. J.* **2022**, *431*, 133359. [[CrossRef](#)]
33. Huang, D.; Wang, K.; Li, L.; Feng, K.; An, N.; Ikeda, S.; Kuang, Y.; Ng, Y.; Jiang, F. 3.17% efficient Cu₂ZnSnS₄-BiVO₄ integrated tandem cell for standalone overall solar water splitting. *Energy Environ. Sci.* **2021**, *14*, 1480–1489. [[CrossRef](#)]
34. Tan, J.; Yang, W.; Oh, Y.; Lee, H.; Park, J.; Boppella, R.; Kim, J.; Moon, J. Fullerene as a Photoelectron Transfer Promoter Enabling Stable TiO₂-Protected Sb₂Se₃ Photocathodes for Photo-Electrochemical Water Splitting. *Adv. Energy Mater.* **2019**, *9*, 1900179. [[CrossRef](#)]
35. Gelderman, K.; Lee, L.; Donne, S.W. Flat-Band Potential of a Semiconductor: Using the Mott-Schottky Equation. *J. Chem. Edu.* **2007**, *84*, 685. [[CrossRef](#)]
36. Liang, G.; Li, Z.; Ishaq, M.; Zheng, Z.; Su, Z.; Ma, H.; Zhang, X.; Fan, P.; Chen, S. Charge Separation Enhancement Enables Record Photocurrent Density in Cu₂ZnSn(S,Se)₄ Photocathodes for Efficient Solar Hydrogen Production. *Adv. Energy Mater.* **2023**, 2300215. [[CrossRef](#)]
37. Beranek, R. Photoelectrochemical methods for the determination of the band edge positions of TiO₂-based nanomaterials. *Adv. Phys. Chem.* **2011**, *2011*, 786759. [[CrossRef](#)]
38. Trasatti, S. The absolute electrode potential: An explanatory note. *Pure Appl. Chem.* **1986**, *58*, 955–966. [[CrossRef](#)]
39. Yu, Z.; Li, C.; Chen, S.; Zheng, Z.; Fan, P.; Tan, M.; Yan, C.; Zhang, X.; Su, Z.; Liang, G. Unveiling the Selenization Reaction Mechanisms in Ambient Air-Processed Highly Efficient Kesterite Solar Cells. *Adv. Energy Mater.* **2023**, 2300521. [[CrossRef](#)]

Disclaimer/Publisher's Note: The statements, opinions and data contained in all publications are solely those of the individual author(s) and contributor(s) and not of MDPI and/or the editor(s). MDPI and/or the editor(s) disclaim responsibility for any injury to people or property resulting from any ideas, methods, instructions or products referred to in the content.